

Infrared Surface Plasmon Resonance Biosensor

Justin W. Cleary^a, Gautam Medhi^a, Robert E. Peale*^a, Walter R. Buchwald^b, Oliver Edwards^c, and
Isaiah Oladeji^d

^aDepartment of Physics, University of Central Florida, Orlando, Florida 32816, USA

^bAir Force Research Laboratory, Sensors Directorate, Hanscom Air Force Base, Massachusetts
01731, USA

^cZyberwear Inc., 2114 New Victor Rd., Ocoee, Florida 34761, USA

^dSisom Thin Films, LLC, 1209 West Gore Street, Orlando, FL 32805, USA

ABSTRACT

A Surface Plasmon Resonance (SPR) biosensor that operates deep into the infrared (3-11 μm wavelengths) is potentially capable of biomolecule recognition based both on selective binding and on characteristic vibrational modes. A goal is to operate specifically at wavelengths where biological analytes are strongly differentiated by their IR absorption spectra and where the refractive index is increased by dispersion. This will provide enhanced sensitivity and selectivity, when biological analytes bind reversibly to biomolecular recognition elements attached to the sensor surface. This paper describes work on the optical and materials aspects of IR surface plasmon resonances. First, three possible coupling schemes are considered: hemicylindrical prisms, triangular prisms, and gratings. Second, materials with plasma frequencies one order of magnitude smaller than for noble metals are considered, including doped semiconductors and semimetals.

Keywords: Biosensor, surface plasmon, plasmonics, grating, infrared, semimetal

1. INTRODUCTION

We are undertaking to develop an instrument for identifying and quantifying bio-molecules, cells, microbes, and their interactions. This instrument will be a Surface Plasmon Resonance (SPR) biosensor, which for the first time can operate deep into the infrared (3-11 μm wavelengths). It will be capable of recognition based both on selective binding and on characteristic vibrational modes. The goal is to operate specifically at wavelengths where biological analytes are strongly differentiated by their IR absorption spectra. In comparison with current commercial visible/near-IR systems, enhanced sensitivity and selectivity are anticipated due to large index changes near characteristic IR absorption features, when biological analytes bind reversibly to biomolecular recognition elements attached to the sensor surface. The overall objective is to enrich and extend the proven SPR biosensor technology, by adding access to a new part of the electromagnetic spectrum. The proposed Infrared Surface Plasmon Resonance Biosensor will have application in life science, electro-analysis, drug discovery, food quality and safety, environmental science, gas-and liquid-phase chemical sensors, forensics, defense, and security.

Biomolecules that adhere to a conducting surface strongly affect the bound electromagnetic waves known as surface plasmon-polaritons (SPP), providing a means for real-time label-free sensing and monitoring of biological entities from molecules to cells. Current commercial systems are based on angle-dependent resonant absorption at the surface of a metal-coated attenuated total reflection (ATR) prism under conditions of total internal reflection. Fig. 1 (left) presents a schematic of the method. A monochromatic near-IR light source is focused through a hemicylindrical prism and optically-contacted sensor chip onto the bottom side of a semi-transparent gold film. The cone of incident p-polarized light is sufficient to include all angles of interest under conditions of total internal reflection. The angular structure of the reflected light is analyzed by an array detector. The top surface of the gold film is functionalized with biomolecule recognition elements that reversibly capture specific analyte biomolecules from the flow channel. This results in a refractive index change within a few 100 nm of the surface. This change is felt by the evanescent field above the surface, causing a shift in the angle at which the surface plasmon resonance absorption emerges in the reflected light. Microfluidics control the flow of tiny volumes of reagents, buffers, and solutions for delivery and release of the analyte

and for regenerating (cleaning) the sensing surface. This method allows biomolecule detection without fluorescent or radioactive labels. It also allows the study of interactions between analyte and bound BRE ligands in real time, giving information on cellular processes.

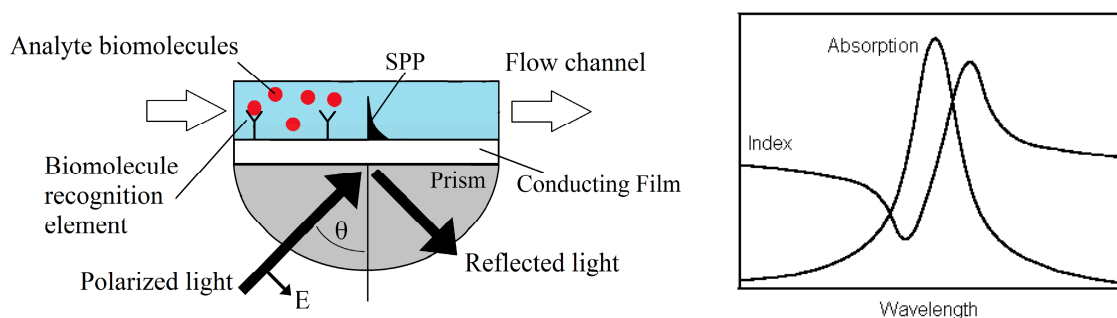


Figure 1. (left) Schematic of conventional SPR Biosensor. (right) Usual relation between refractive index and absorption line.

For operation at IR wavelengths (3 to 11 μm), one might use (for example) a quantum cascade laser, a silicon prism, a sensor chip with doped silicon as the conducting surface, all-silicon microfluidic channels & controls, and an IR 2-D array detector. In comparison to gold, the lower plasma frequency of doped silicon allows SPP fields to be confined to heights above the sensor surface of the order of 1 μm , so that there is good spatial overlap between fields and the biological analyte-ligand. The high mobility of silicon in principle allows for sharp resonances.

A number of considerations compel this effort. The first is that large characteristic changes for the refractive index are expected near the characteristic IR vibrational absorption lines. Fig. 1 (right) shows the usual relation between refractive index and absorption, where a sharp upturn in refractive index occurs on the long-wave side of an absorption line. A larger analyte index will give a larger SPP resonance shift, thus improving sensitivity.

The second consideration is that different biomolecules have different absorption features in the IR, so that the response of the SPR biosensor will be different depending on the species of bound analyte. This is in sharp contrast to conventional (VIS-NIR) SPR biosensors, where the response is nearly independent of the biomolecular species, since there are no strong absorption features in the near-IR. Thus, an IR SPR biosensor is anticipated to yield enhanced specificity. This effect can be enhanced by using two or more channels with different IR wavelengths, a clear possibility given the design tunability of quantum cascade lasers.

A third consideration in favor of our innovation is that semiconductor quantum cascade lasers have become available throughout the IR. These are more monochromatic than the near-IR LEDs used in conventional SPR biosensors, which will yield angularly sharper resonances and thus higher sensitivity. They are design tunable over the complete infrared, operate at room temperature, and are very stable.

Since optical and SPR properties of materials differ significantly in mid-IR, the transition from the near-IR requires a change in the conducting material that hosts the SPP and in both the material and design of the SPP coupler. This paper describes work on these optical and materials aspects. First, three possible coupling schemes are considered: hemicylindrical prisms, triangular prisms, and gratings. Second, materials with plasma frequencies one order of magnitude smaller than for noble metals are considered, including doped semiconductors and semimetals.

2. EXPERIMENT AND RESULTS

2.1 IR SPP coupling schemes

For investigating SPP coupling schemes, we use traditional gold conducting layers as the SPP host. Then resonances are sharp, which facilitates the investigation of the coupler. Note, however, that the extent of the SPP mode above a gold surface is about 100 μm at wavelength of 10 μm ¹. Hence, gold is ineffective as an SPP host for an IR biosensor due to poor overlap between SPP mode and any likely biological analyte. Different SPP host materials are considered below.

The first coupling scheme that we consider is the hemicylindrical prism (Fig. 2, left). This choice is based on current art in the visible/near-IR spectral range. The value of this type of prism is that there is no limitation to the range for the angle of incidence, and the angle of incidence is unchanged by refraction, simplifying the analysis. The disadvantage, as we will show, is that IR prism materials with high transmittance also have high refractive index, forming a high Q optical cavity with Fabry-Perot resonance artifacts.

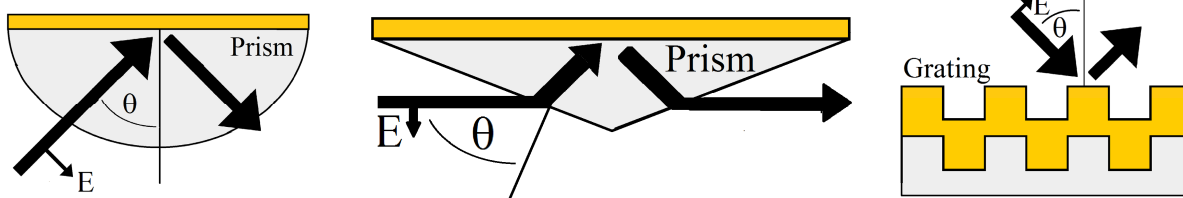


Figure 2. IR-to-SPP couplers. (left) hemicylindrical prism; (center) triangular prism; (right) diffraction grating. Incident and reflected rays are shown symmetric about the surface normal. The surfaces are coated with a thin gold layer as SPP host.

The second coupling scheme we consider is the triangular prism. The advantage is that there are no optical cavity effects. A disadvantage is that, due to refraction in the high index IR material, the range of accessible incidence angles is limited. Moreover, the relation between the angles within and outside the prism is non-linear, complicating the analysis.

The third coupling scheme that we investigate is the diffraction grating. Advantages are that these are easy to fabricate photolithographically, the thickness of the conducting layer is arbitrary as long as it is optically thick, and the incident light passes through no lossy material. A disadvantage is that multiple resonances occur in the reflectance spectra.

2.1.1 Hemicylindrical prism

The material used for the prism needs to have low loss at the IR wavelengths considered. Our initial experiments used a CO₂ laser ($\sim 10 \mu\text{m}$ wavelength or $\sim 1000 \text{ cm}^{-1}$), where Ge has low loss². Hence, first hemicylindrical prisms were fabricated from Ge. Silicon was also used because it is cheap, readily available, and for its well developed processing know-how. The loss for Si is higher than for Ge, however.²

Fig. 3 presents photographs of in-house prism-fabrication (left), two finished hemi-cylindrical semiconductor prisms (center), and one commercial Si ATR prism (right). The in-house fabrication used a hollow diamond-tipped drill bit which cuts out a cylindrical shape. The outer surface of the cylinder was hand polished using silicon carbide grit. The polished cylinder was split with a diamond saw and the flat surface hand polished. The left prism in Fig. 3 (center) is made from germanium and the right one from silicon (resistivity $> 200 \Omega\text{-cm}$). All three prisms in Fig. 3 have been gold coated on their flat surfaces.

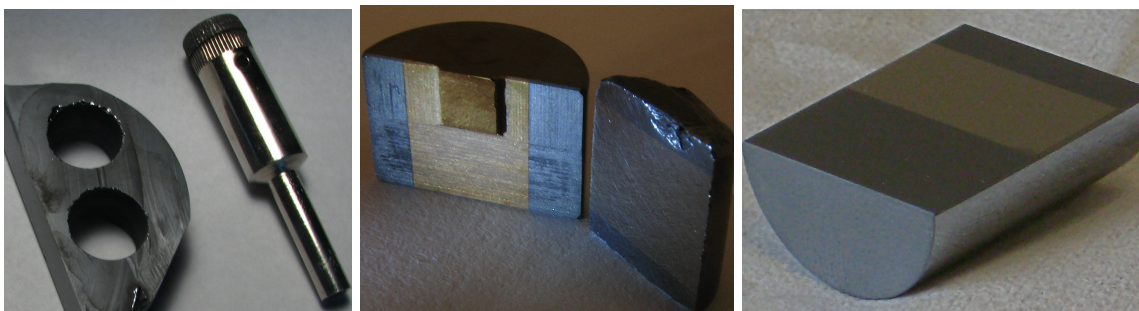


Figure 3. (left) Silicon slab with holes cut using diamond drill bit. (center) Ge and Si hemicylindrical prisms with gold coatings, 1 cm diameter. (right) Commercial Si ATR prism (Korth Kristalle GMBH).

The experiment follows the schematic of Fig. 2 (left), using a goniometer to vary the angle of incidence while tracking the reflected ray with a point detector. The calculated resonance angle for Au on Ge is 14.5 deg, which is very

close to the critical angle for total internal reflection. The experimental set up used a p-polarized CO₂ laser operating at 9.552 μm wavelength (a minimum in the Si absorbance²), chopped at 230 Hz, detected with a 77 K HgCdTe detector, and synchronously amplified (Stanford SR830 lock-in amplifier).

The reflectance data are presented in Fig. 4 (left). The data are dominated by fast and slow oscillations, and no resonance is detected near 14.5 deg. The oscillations are explained as follows. The prism can never be perfectly cylindrical nor can it be cut perfectly on a diameter, so that the internal path length changes with the angle of incidence. A high Q cavity is formed inside the high-index prism between the two spherical surfaces, resulting in high-visibility interference fringes. These oscillations obscure the resonance and are the main disadvantage of hemicylindrical prisms for our IR biosensor application.

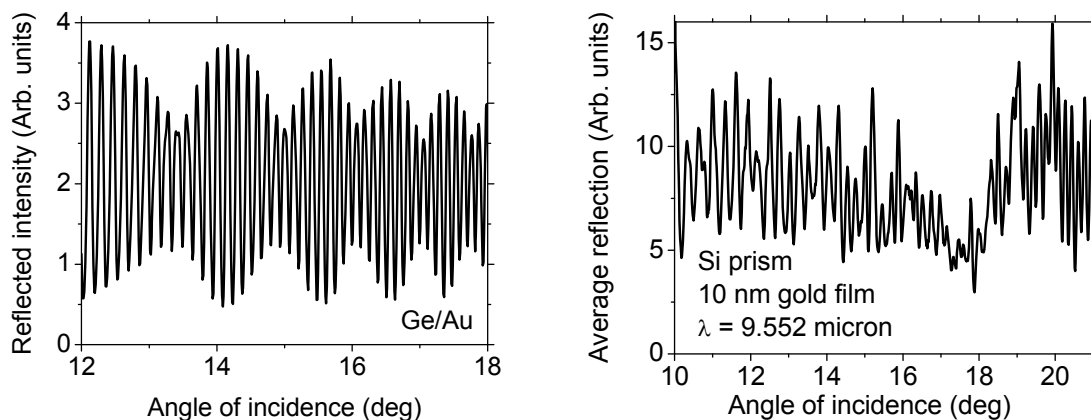


Figure 4. (left) Measured reflectance vs. angle of incidence for Ge hemicylindrical prism. (right) Resonance absorption due to creation of SPP for Si prism with 10 nm gold film. Interference fringes partially obscure the resonance. This data contains more noise than for Ge due to the higher loss and lower throughput in Si.

The angular reflectance spectrum for the homemade Si prism is presented in Fig. 4 (right). The film was formed by depositing 5 nm of Ti, to promote sticking, followed by 5 nm of Au. Here a resonance is observed close to the expected 17 deg. Where the absorption is strongest, the fringes are weakest, due to the reduction of the cavity Q. The resonance is much broader than we calculate using Fresnel equations, and it is shifted to higher angles of incidence. The commercially-prepared ATR prism turns out to be just as bad. The difficulty in obtaining a clean sharp resonance spectrum without interference fringes suggests that semiconductor hemicylindrical prisms are a poor approach to the LWIR SPR biosensor application.

2.1.2 Triangular prism coupler

The advantage of a triangular prism coupler is that there are no internal cavity resonances to cause oscillations in the angular reflection spectrum. The disadvantage is that the prism angle for the high index IR material must be large in order to access the desired angles of incidence at the sensor surface. Prisms with such angles are not items of commerce and will have to be specially manufactured. Fig. 5 presents scale drawings of a theoretically optimum Si prism. The range of accessible and useful angles is indicated by the presentation of the two limits. Table I gives the relevant angles for Si, Ge, ZnSe, and ZnS prisms.

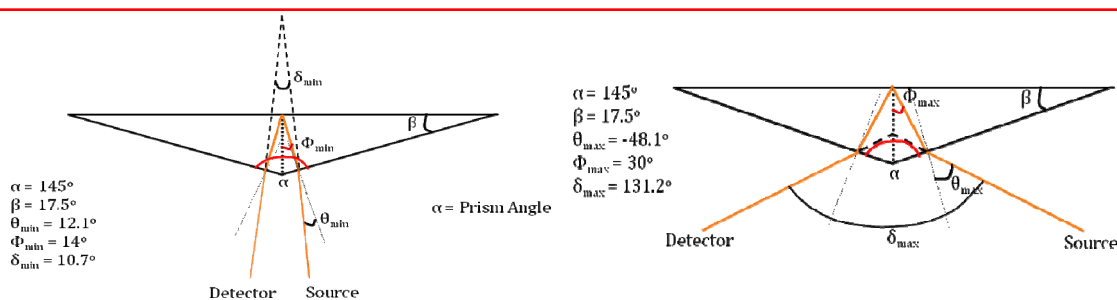


Figure 5. Ray diagram of silicon prism. Two configurations are shown. (left) Minimum, (right) maximum incident angle at the base. All angles are in degrees.

Table I. Prism design data for four IR materials

Material	Critical Angle	Desired incidence angular range at base		Ideal α	δ_{\min}	δ_{\max}	θ_{\min}	θ_{\max}
		Φ_{\min}	Φ_{\max}					
Si	16.9	14	30	145	10.7	131.2	12.1	-48.1
Ge	14.5	12	27	152	11.9	156.2	8.1	-64.1
ZnSe	20.3	17	33	135	12.8	108.6	16.1	-31.7
ZnS	24.6	22	37	115	13.2	86.7	25.9	-10.8

2.1.3 Grating couplers

Gratings are well known as couplers between photons and SPPs. They function by shifting the incident photon wavevector by integer multiples m of $2\pi/a$, where a is the grating period. This allows intersection between photon and SPP dispersion curves so that momentum may be conserved during the transition (surface electromagnetic waves travel slower than free space ones). A feature of this kind of coupler is that there are multiple resonances due to the multiple units of grating momentum that may be added.

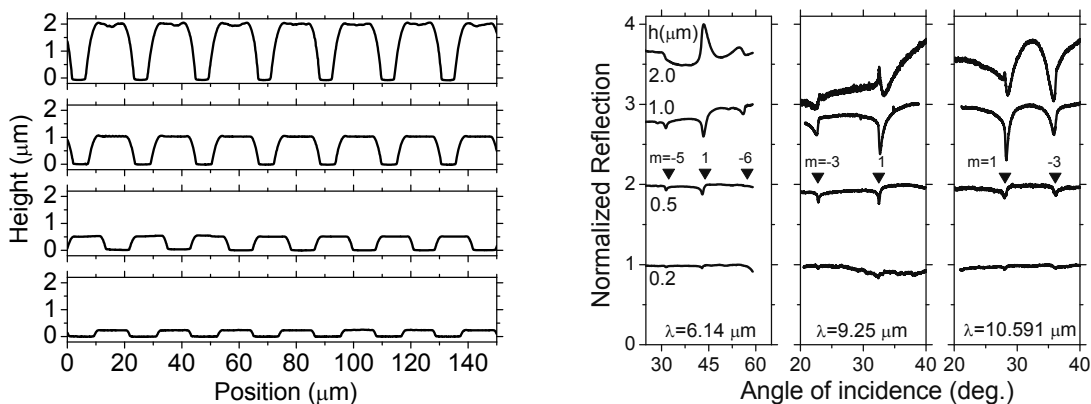


Figure 6 (left) Gold grating profiles. (right) Resonances in specular reflection from gold gratings for three wavelengths and different grating amplitudes h . Resonance orders m are indicated.

Gratings of 20 μm period and different amplitudes were formed by photolithography and plasma etching in silicon. Then an optically thick layer of gold was deposited on top of the lamellar structure. Profiles presented in Fig. 6

(left) show that the actual period is $21.4 \pm 0.1 \mu\text{m}$. The measured grating amplitudes are 0.24, 0.51, 1.05, and $2.1 \mu\text{m}$. Fig. 6 (right) presents the angular reflectance spectra for the gold gratings measured using either a quantum cascade laser or CO_2 laser with a power meter or 77 K HgCdTe detector. Symbols indicate the expected resonance positions, which are labeled by their m values. Gratings of $\sim 1 \mu\text{m}$ amplitude give the strongest resonances, but the resonances for smaller amplitudes are sharper.

The resonant dips in grating reflection have two origins. The first and desired one is the conversion of power from the laser beam into surface plasmons supported by the conducting surface. The second occurs even for dielectric gratings, when diffraction orders exit or emerge at grazing incidence, causing a change in the specular beam intensity. These ‘‘Rayleigh resonances’’ are weaker and broader, but they coincide with the SPP resonances, which may lead to some degree of interference for the biosensor application. However, we do not observe the Rayleigh resonances at all for uncoated Si gratings for the given range of grating amplitudes.

2.2 Infrared SPP host materials

The objective here is to identify conductors with plasma frequencies one order smaller than for noble metals, which requires carrier concentrations two orders smaller. Equivalently, the real part of the permittivity should go negative at a suitable mid-IR wavelength. At the same time, the imaginary part of the permittivity should be sufficiently small, so that the resonances will be sharp.

A number of different conductors have been considered. We have considered metal-silicides^{1,3-4} for SPP hosts. However, these have carrier concentrations only one order smaller than metals. In this work, we first considered heavily-doped semiconductors. We investigated commercial heavily doped wafers and we prepared silicon doped by ion-implantation or diffusion. Ellipsometry has shown that it is difficult to achieve a plasma frequency corresponding to wavelengths much shorter than $10 \mu\text{m}$. The theoretical considerations for doped-silicon have been published.¹ Secondly, we considered chemical-bath deposited CuSnS. Ellipsometry shows that this material is suitable for our application. After semiconductors, we considered semimetals. These are graphite, Bi, Sb, and As. The last was considered too poisonous to work with. Samples of the first three were prepared and studied.

Fig. 7 presents permittivity from ellipsometry measurements on optically thick films of Pd_2Si , Graphite, and Sb. For doped-Si, the presented permittivity values were calculated based on the Drude model, and the Au data are published values.⁵ Fig. 8 shows permittivity from ellipsometry measurements of CuSnS and molybdenum. These data will be discussed in the following sections.

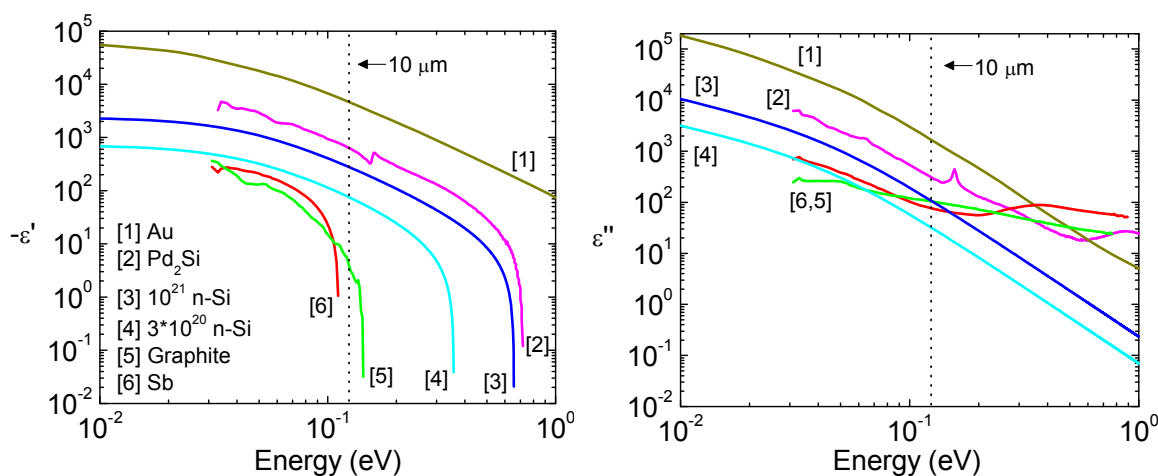


Figure 7. Ellipsometric permittivity spectra for Pd_2Si , Graphite, and Sb. The spectra for n-type doped-Si (10^{21} and $3 \times 10^{20} \text{ cm}^{-3}$) are calculated from the Drude model. The spectrum for Au is from published data.⁵ The energy corresponding to $10 \mu\text{m}$ free space wavelength is indicated.

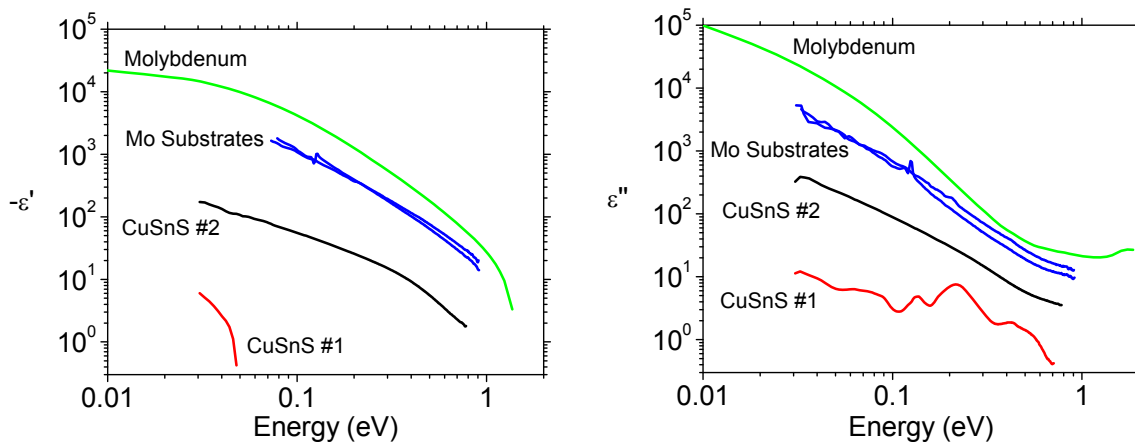


Figure 8. Permittivity of CuSnS deposited on molybdenum, compared with that bare molybdenum, published⁶ and measured. (left) real part. (right) imaginary part.

2.2.1 Doped-Si

We heavily-doped one surface of double-side polished un-doped silicon wafers. The starting wafer material was high-resistivity silicon. Implantation of phosphorus was performed by Leonard Kroko, Inc. The ion implant schedule was a dose (ions/cm²) of 9.5×10^{15} at 60 keV followed by a 2.5×10^{15} dose at 30 keV. A 15 minute 900 C post-implant anneal was performed. Diffusion was also performed at the University of Central Florida via continuous source deposition during the 40 min at 950 C. Secondary ion mass spectroscopy (SIMS) for the implanted sample shows that the ion concentration follows the calculated (TRIM) curve very closely, reaching a peak concentration close to 10^{21} cm⁻³ to a depth of at least 100 nm. The actual carrier concentration is lower since not all implanted ions will be electrically activated even after annealing. SIMS analysis of the diffused sample indicates a maximum dopant concentration near the surface of about 2×10^{20} cm⁻³. Complex permittivity was measured by IR ellipsometry. Only the diffused sample has a negative ϵ' in any part of the IR wavelength space (goes slightly negative around 10.6 μ m wavelength). This suggests that though the implanted sample has the higher ion concentration, it actually has the lower carrier concentration. Since a negative ϵ' is required to sustain an SPP, these data indicate that neither sample has sufficient carrier concentration to support SPPs in the wavelength range of the CO₂ laser. Moreover, even where $\epsilon' < 0$, we have $\epsilon'' > |\epsilon'|$, so that any resonance should be broad.

Fig. 9 (left) presents calculated resonance spectra for n-Si with different carrier concentrations at a wavelength of 9.55 μ m. The prism method was used with permittivity data from Fig. 7 and also Drude permittivity for concentration 10^{20} cm⁻³. The calculations show that to see a clear resonance, we need at least 3×10^{20} cm⁻³ electrons. To see a sharp resonance, we need to approach 10^{21} cm⁻³, which is near the limit of possible doping. Attempt to observe a resonance with our own samples was unsuccessful, in agreement with the predictions from SIMS and ellipsometry. We conclude that it will be difficult to obtain surface-doped silicon with sufficient carrier concentration to observe SPP resonances at wavelengths less than or equal to 10 μ m by the prism method.

Fig. 9 (right) presents calculated angular reflectance spectra for the doped silicon and CuSnS gratings using the method in Ref. 7 and the permittivity data in Figs. 7-8. Here, the Si resonances are sharper than for the prism and a resonance occurs for a doping concentration as low as 10^{20} cm⁻³. This suggests that the grating coupler is preferable to the prism method, as it allows the use of achievable silicon doping levels.

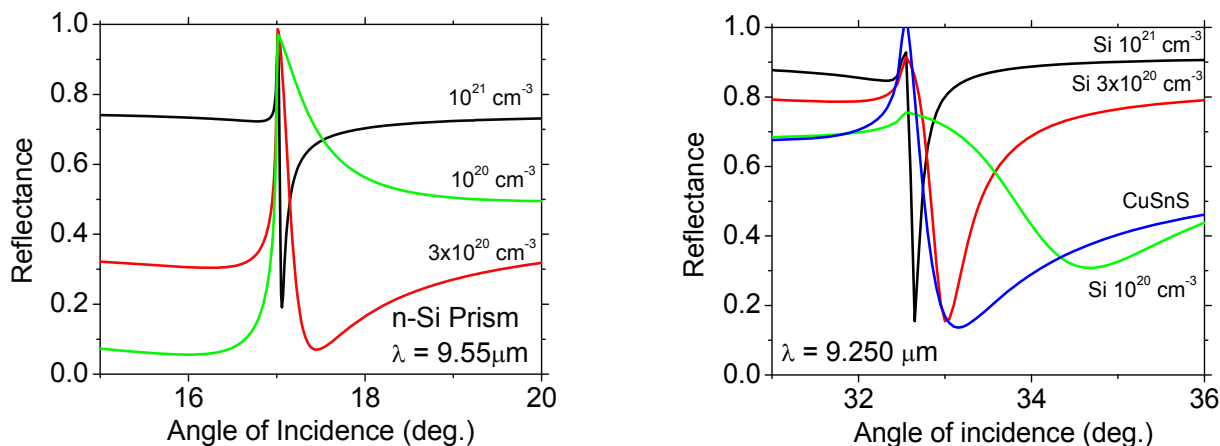


Figure 9. (left) Calculated internal reflectance spectra for a 100 nm thick doped layer on a Si prism surface for three different carrier concentrations. The bulk of the prism is un-doped. The wavelength is chosen where silicon has the least absorption within the CO₂ laser range. (right) Calculated angular reflectance spectra for silicon and CuSnS gratings of optimized height and 20 μm period.

2.2.2 CuSnS

CuSnS is a semiconductor that may be very heavily doped and deposited on a suitable substrate by chemical bath deposition. Our samples were deposited on molybdenum substrates by SISOM Thin Films. CuSnS sample #1 has film thickness $> 1 \mu\text{m}$ while CuSnS sample #2 has film thickness $> 2 \mu\text{m}$. As shown in Fig. 8, at 10 μm wavelength (0.124 eV), the CuSnS #1 still has positive real part of permittivity, but CuSnS #2 gives $\epsilon' = -44$ and $\epsilon'' = 64$. The bare molybdenum substrate was also measured and shows a factor of 2-3 smaller permittivities than the published values,⁶ though they are still clearly metallic.

The plan to make grating couplers with an active CuSnS surface is based on patterning of the molybdenum substrate with a 20 μm period lamellar structure followed by CuSnS chemical bath deposition. Fig. 10 (left) presents profiles of some substrates that were so patterned by plasma etch with a photolithographic mask. The grating depths were determined to be 0.37, 0.38, and 2.9 μm . Angular reflectance spectra were collected on the patterned molybdenum substrates (Fig. 10, right) as background information before the CuSnS depositions. Resonances are observed near the expected positions, indicated by symbols.

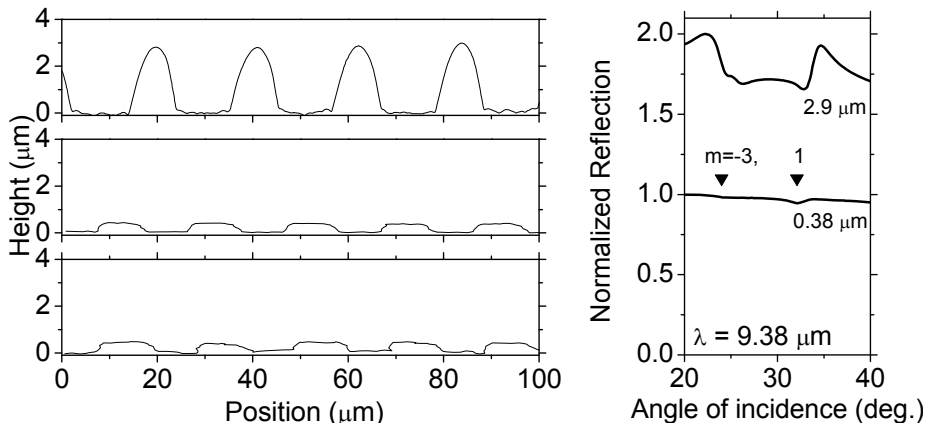


Figure 10. (left) Etched molybdenum substrate grating profiles. (right) Angular reflectance spectra of molybdenum gratings showing SPP resonances with different grating heights indicated. Symbols give calculated resonance positions.

In anticipation of measurements on CuSnS-coated gratings, we performed calculations of the expected reflection resonances according to the theory of Ref. 7 using measured permittivity values. The calculated angular reflectance spectrum for a CuSnS grating is presented in Fig. 9 (right) and compared with doped silicon. The resonance is reasonably deep and well defined.

2.2.3 Graphite

A high purity graphite wafer, 20 mm x 20 mm x 1 mm, SPI-3 grade, PN=449HP-AB was purchased from 2spi.com. The in-plane resistivity is $40 \mu\Omega\text{-cm}$, which is 20 times higher than Au. Our ellipsometric permittivity spectra (Fig. 7) agree with the published values.⁸ The real part is negative in the wavelength range 8.6 to $56 \mu\text{m}$. At $10 \mu\text{m}$, our measurement yields $\epsilon' = -3.92$ and $\epsilon'' = 104.0$, where the negative real part suggests that graphite can support a LWIR SPP. The large ϵ'' value for graphite at $10 \mu\text{m}$ wavelength suggests that the resonances may be broad. However, calculation⁷ shows a reasonably sharp and deep resonance for an optimized grating height (Fig. 11, left). The calculated penetration depth for the SPP field into air above the graphite surface is $23 \mu\text{m}$ at $10 \mu\text{m}$ wavelength. This is larger than for heavily-doped silicon but smaller than for silicides or noble metals. Thus graphite has reasonable prospects as an SPP host for a LWIR SPR biosensor. Moreover, the knowledge of binding for biomolecules to graphite is extensive.

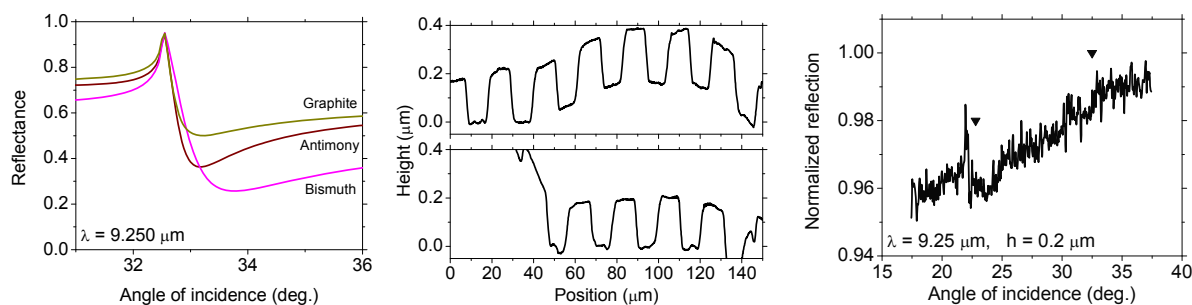


Figure 11. Calculated angular reflectance spectra for a semi-metal gratings (Sb, Bi and graphite) of optimized amplitude, $20 \mu\text{m}$ period, and $9.25 \mu\text{m}$ wavelength. (center) Measured grating profiles for a patterned graphite wafer. (right) Measured angular reflectance spectrum for the graphite grating.

The graphite wafer was patterned and etched. The measured profiles in two regions of the same wafer are presented in Fig. 11 (center). The measured period is $21.3 \mu\text{m}$, and the measured amplitude is $0.22 \mu\text{m}$. The grating pattern is superimposed on a longer wavelength undulation that was intrinsic to the as-delivered wafer. This undulation caused the reflectance to be somewhat diffuse, which worsened the signal to noise ratio and somewhat masked the expected resonances (Fig. 11, right). Nevertheless, small features are seen near the expected positions indicated by symbols.

2.2.4 Antimony

Antimony has equal electron and hole densities of $5 \times 10^{19} \text{cm}^{-3}$ and a resistivity of $39 \mu\Omega\text{-cm}$,⁹ which is comparable to graphite. Its relaxation time $\tau = m/(\rho n e^2)$ of 1.6ps is significantly larger than for gold (0.03ps). It vaporizes at low temperature, with melting point 600C and boiling point 1587C . Permittivity spectra in the mid-infrared are plotted in Fig. 7. Negative values of ϵ' appear only for wavelengths longer than $10 \mu\text{m}$. (Our Sb permittivity spectra generally agree with Ref. 10 except that our curve is shifted to slightly lower energies.) Yet the calculated angular resonance spectrum for reflection from an Sb grating with optimized groove amplitude (Fig. 11, left) shows a clear resonance, which is better defined than for graphite.

Antimony was evaporated onto patterned silicon wafers. The nominal Sb layer thickness was $1.2 \mu\text{m}$ (determined by a crystal monitor at the time of deposition), which was estimated to be larger than the LWIR skin depth by a factor of ~ 5 . The measured profiles are presented in Fig. 12 (left), where the period is found to be $21.4 \mu\text{m}$ and the amplitudes are $0.24, 0.54, 1.05,$ and $2.03 \mu\text{m}$. Resonances are observed at 6.14 and $9.38 \mu\text{m}$ (Fig. 12, center) for

amplitudes greater than 0.5 μm using quantum cascade lasers. Resonances measured using two different CO_2 laser lines (Fig. 12, right) confirm these observations.

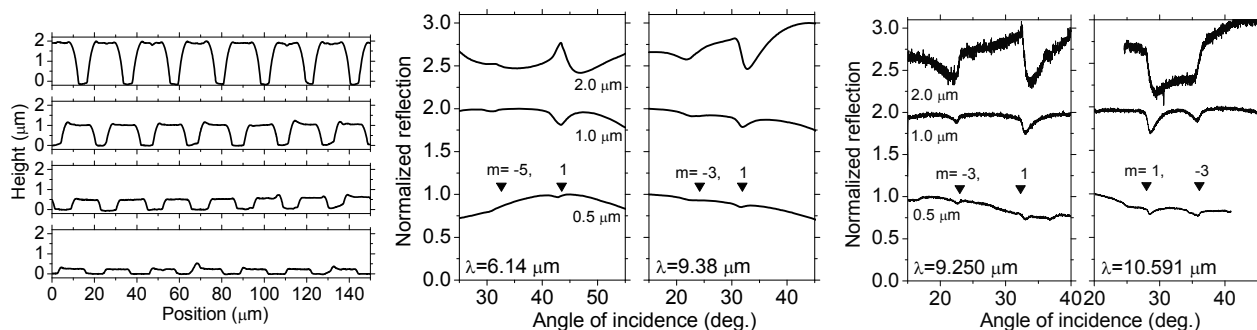


Figure 12. (left) Antimony grating profiles. (center) Angular reflectance spectra at 6.14 and 9.38 μm QCL wavelengths. (right) Angular reflectance spectra for Sb gratings at CO_2 laser wavelengths.

2.2.5 Bismuth

Measured bismuth permittivity spectra are compared with published values in Fig. 13. Our measurements (smooth curve) show that ϵ' is positive out to wavelengths of 30 μm . (The oscillations we observe appear to be continued in the short-wave published data.) Bismuth was evaporated onto patterned silicon to produce gratings with period 21.4 μm and amplitudes 0.24, 0.54, 1.02, and 2.07 μm (Fig. 14, left). The nominal Bi layer thickness was 1.7 μm . Contrary to expectations from the permittivity data, Bi gratings show clear SPP resonances (Fig. 14 center and right) comparable to those observed for Sb.

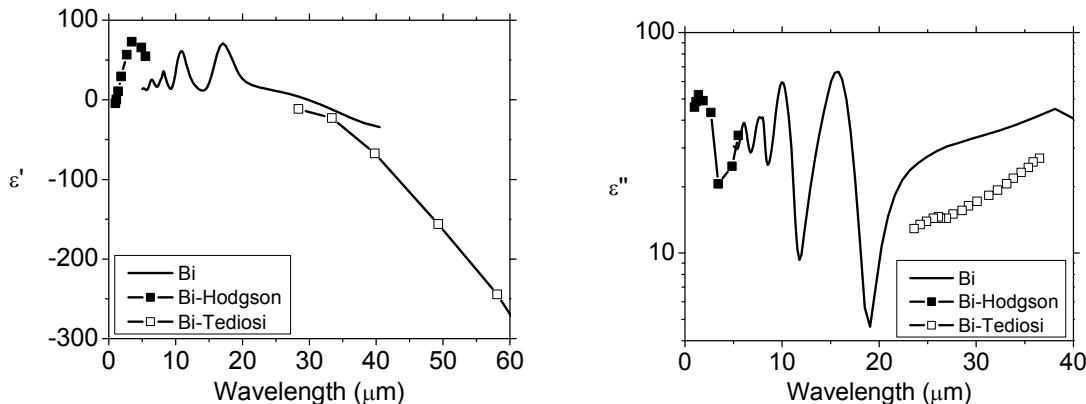


Figure 13. Ellipsometric permittivity spectra for Bi compared to those of Refs. 11-12. Permittivity from reference 12 is calculated based from the Drude model from conductivity data.

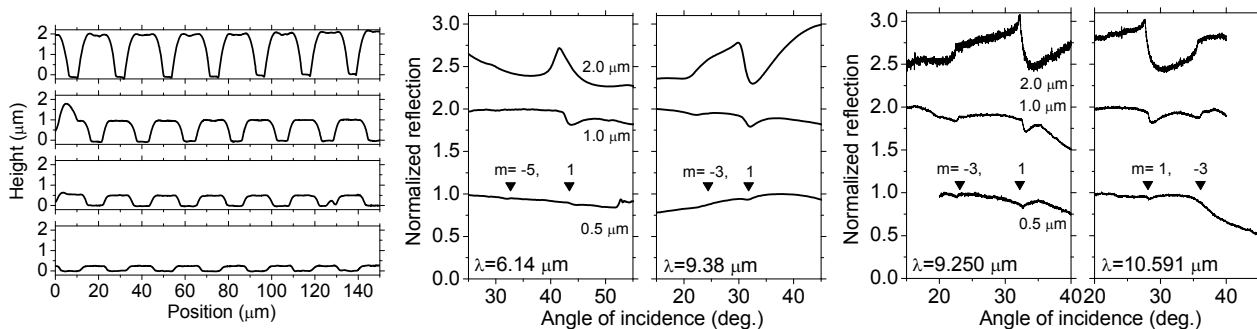


Figure 14. (left) Bismuth grating profiles. (center) Angular reflectance spectra at 6.14 and 9.38 μm QCL wavelengths. (right) Angular reflectance spectra for Bi gratings at CO_2 laser wavelengths for the indicated grating heights.

3. SUMMARY

This paper described work on the optical and materials aspects of IR surface plasmon resonances. Three possible coupling schemes for an infrared surface plasmon resonance biosensor were considered: hemicylindrical prisms, triangular prisms, and gratings. The latter two appear to have the most promise. The triangular prism coupling scheme should be free from the Fabry-Perot oscillations observed when using the hemicylindrical prism coupler. Gratings as SPP couplers are the easiest to produce and can give sharp resonances. Materials with plasma frequencies one order of magnitude smaller than for noble metals were considered, including doped semiconductors and semimetals. Highly doped-Si was prepared by ion-implantation and diffusion. Ellipsometry measurements suggest that the achieved carrier concentration is too low to support SPPs below 10 micron wavelength for prism couplers, though grating couplers might still be used. Permittivity for CuSnS suggest that it is a suitable IR SPP host. All the semi-metals considered show SPP resonances for grating couplers and thus have reasonable prospects as SPP hosts for LWIR SPR biosensors.

ACKNOWLEDGMENTS

This project is supported by an NSF Phase I SBIR and by an AFOSR grant FA95501010030 (Gernot Pomrenke PM). We thank Vinit Todi and Prof. Kalpathy Sundaram at UCF for the silicon diffusion. We thank Prof. Glenn Boreman for use of the IR ellipsometer.

REFERENCES

- [1] R. Soref, R. E. Peale and W. Buchwald, "Longwave plasmonics on doped silicon and silicides," *Opt. Express* 16, 6507-6514 (2008).
- [2] R. A. Soref, S. Emelett and W. Buchwald, "Silicon Waveguided Components for the Long-Wave Infrared," *J. Opt. Soc. Am. A* 8, 840-848 (2006).
- [3] J. W. Cleary, R. E. Peale, D. J. Shelton, G. D. Boreman, C. W. Smith, M. Ishigami, R. Soref, A. Drehman, and W.R. Buchwald, "IR permittivities for silicides and doped silicon," accepted to *J. Opt. Soc. Am. B* (2010).
- [4] J. Cleary, R. E. Peale, D. Shelton, G. Boreman, R. Soref, W. Buchwald, "Silicides for infrared surface plasmon resonance biosensors," *Proc. Mat. Res. Soc.* 1133-AA10-03 (2008).
- [5] M. A. Ordal, R. J. Bell, R. W. Alexander Jr., L. L. Long and M. R. Querry, "Optical properties of Au, Ni, and Pb at submillimeter wavelengths," *Appl. Opt.* 26, 744-752 (1987).
- [6] M. A. Ordal, R. J. Bell, R. W. Alexander Jr., L. A. Newquist, and M. R. Querry, "Optical properties of Al, Fe, Ti, Ta, W, and Mo at submillimeter wavelengths," *Appl. Opt.* 27, 1203-1209 (1988).
- [7] J. W. Cleary, G. Medhi, R. E. Peale, and W. R. Buchwald, "Long-wave infrared surface plasmon grating coupler," submitted to *Appl. Opt.* (2010).
- [8] H. R. Phillip, "Infrared optical properties of Graphite," *Phys. Rev. B* 16, 2896-2900 (1977).
- [9] N. W. Ashcroft and N. D. Mermin, [Solid State Physics], Saunders College, Philadelphia (1976).
- [10] I. N. Shklyarevskii, A. A. Avdeenki, and V. G. Padalka, "Measurements of the Optical Constants of Antimony in the Infrared Region of the Spectrum at Temperatures of 290° and 110°," *Opt. Spectrosc.* 6, 336 (1959).
- [11] J. N. Hodgson, "The infra-red properties of Bismuth," *Proc. Phys. Soc. B* 67, 269-270 (1954).
- [12] R. Tediosi, N. P. Armitage, E. Giannini, and D. V. Marel, "Charge carrier interaction with a purely electronic collective mode: plasmarons and the infrared response of elemental bismuth," *Phys. Rev. Lett.* 99, 016406 (2007).